Keywords: ammonia, ammonia-combustion, engine relevant conditions, pre-chamber, carbon free combustion, emissions, high IMEP, high BMEP, optical investigation

The GHG reduction potential of high-IMEP pure ammonia combustion

Silas Wüthrich, Patrick Albrecht, Patrick Cartier, Prof. Kai Herrmann

Institute of Thermal and Fluid Engineering (ITFE), University of Applied Sciences and Arts Northwestern Switzerland (FHNW)

https://doi.org/10.18453/rosdok_id00004647

Abstract

Ammonia as fuel has been widely discussed in the marine sector during the last years. Since ammonia as fuel poses major challenges in combustion, it is common to apply a dual-fuel combustion process, which requires a second fuel, typically diesel, to start the combustion. However, to further reduce greenhouse gas (GHG) emissions, the need for a carbon-based pilot fuel should be eliminated by applying a combustion scheme based on a single carbon-free fuel that maintains high engine efficiency and power output while keeping GHG-related emissions such as nitrous oxide (N_2O) low.

For ammonia, the most commonly used combustion process to date is based on a premixed charge of ammonia ignited by a pilot injection of a carbon-based fuel. This well controllable solution allows a wide range of ammonia / pilot fuel share ratios – such engines are even capable of running on 100% pilot (diesel) fuel only. This high fuel flexibility ensures a secure fuel supply from common suppliers around the world. A more sophisticated approach, in which directly injected ammonia is ignited by pilot injection of a carbon-based fuel, resulting in a diesel-like combustion process, is planned to be used in large-bore two-stroke engines. However, this approach also relies on a small quantity of carbon-based pilot fuel to ensure safe and stable ammonia combustion.

This paper presents research into an ammonia combustion process that does not require a pilot injection and therefore allows for 100% carbon-free operation of such combustion engines. Here, a small portion of an ammonia/air mixture at stoichiometric conditions is ignited in a pre-chamber. The resulting hot combustion gases then form a reactive jet, which enters the main chamber to ignite the premixed main charge at operating point specific air/ammonia equivalence ratios (λ). This combustion process has been applied over a wide range of air-fuel equivalence ratios (λ = 0.8 - 2.0) and different IMEP (up to 27 bar). The research was carried out using an optical engine test facility equipped with exhaust gas measurement. Simultaneously applied high-speed Schlieren and OH* chemiluminescence measurements allow the combustion process to be studied in terms of the (optical) start of ignition, the flame propagation speed, and other characteristics.

A high IMEP, completely carbon free combustion process has been realized, including characterization of heat release, ignition delay, start of combustion, flame propagation speed and pollutant emission

formation for marine engine relevant conditions. The effect of the very low laminar flame speed of ammonia is offset by the additional turbulence created by the reactive jet from the pre-chamber, suggesting that this carbon-free combustion process may be applicable to medium-speed engines as well. In addition, the experiments also provide some insight into the challenge of knocking cycles and lube oil induced pre-ignition events. On the emissions side, the critical formation of nitrous oxide (N_2O) has been studied and the overall GHG reduction potential for this type of combustion process has been assessed.

1. Introduction

The goal of a carbon-neutral society is set out in the Paris Agreement, a legally binding international treaty on climate change, which aims to keep the global average temperature increase well below 2 °C above pre-industrial levels and to step up efforts to limit the temperature increase to 1.5 °C [1]. While the Paris Agreement is mainly aimed at land-based applications, the International Maritime Organization (IMO) targets the greenhouse gas (GHG) reduction strategy for international shipping. Overall, it is imperative that both private and industrial sectors reduce their greenhouse gas emissions towards zero over the course of this century. Wherever possible, electrification based on renewable energies is the most efficient approach to achieve this goal.

On the other hand, due to the limited energy density of batteries, direct use of electricity is limited or not possible in certain applications within industrial sectors. This is particularly true for the marine sector, where – apart from certain niche applications such as ferries or short sea shipping – the switch from fossil to renewable fuels is the most promising options for decarbonization. Since large internal combustion engines (ICE) will continue to play a role for marine propulsion, the transition from fossil fuels to sustainable energy carriers is one of the necessities in view of reducing GHG emissions to keep global warming within tolerable limits.

Various technology paths for ICE and fuel systems for future propulsion of ships have been investigated. For the substitution of fossil fuels, ammonia or methanol were announced as potential candidates for an economically feasible route to decarbonization [2]. Of course, these fuels must be produced via renewable energy, and only ammonia can be considered as completely CO_2-free. Since methanol still contains carbon, the CO_2 needed for production must come from non-fossil sources (direct air capture) to be considered carbon-neutral. All possible options regarding non-fossil fuels – including "green" hydrogen for certain applications – have advantages and disadvantages in terms of scope, handling, efficiency, cost, environmental risks, etc. In particular, the use of ammonia has recently gained increasing attention and is being touted by various stakeholders as one of the most promising future fuels. Various studies have investigated the potential for application in marine shipping from a cost and production point of view [3-8]. Although ammonia is a well-known product since centuries, it has mainly been used to produce fertilizers. In terms of its use as an engine fuel, a transition phase up to 2050 is expected. In the current decade, the share of liquefied natural gas (LNG) will probably still increase before the desired transition to methanol or ammonia takes place. Even if the use of sustainable fuels produced by the synthesis of renewable energies (Power-to-X or synfuels) or from the processing of suitable biological wastes and residues (biofuels) is mandatory, the use of LNG as a marine fuel will probably still be a matter of course in a transition phase over the next decade and beyond.

Current concepts of gas engines are seen as good basis for future solutions designed for operation on such alternative fuels. Even though ammonia fuel application for IC engines is not new, the conversion still providing comparable efficiency and guaranteeing reliable operation, poses certain challenges in terms of ignition concepts and combustion properties. A range of involved complex processes such as flow field conditions, mixing properties, ignition, combustion onset, and flame propagation must be considered. Whereas the upcoming low-speed two-stroke ammonia engines will use a pilot fuel ignited direct injected ammonia combustion scheme (diesel-like) this work focusses on a 100% carbon free combustion without requiring a carbon-based pilot fuel. An optically accessible experimental test facility providing engine relevant operation conditions was used to fundamentally examine premixed

homogeneous combustion ignited by an actively filled pre-chamber. The investigations include typical operating conditions as well as very high engine loads for marine engines with compression temperatures around 950 K and peak pressures up to 300 bar and beyond. The influence of different operating parameters such as mixture charge composition or boost-pressure variations has been investigated. Insight into the thermo-chemical processes of combustion in terms of ignition delay, combustion onset, flame propagation speed, heat release, and exhaust gas composition will be provided.

2. Experimental setup, test execution and analysis

The optically accessible test facility *Flex-OeCoS* enables the examination of premixed pilot fuel ignited dual-fuel combustion processes in a range of IC engine relevant operational parameters [9]. Acquisition of crank-angle resolved operating conditions in terms of precise pressure as well as temperature measurements (by fine-wire thermocouples at different locations), and turbulent flow field determination (by means of high-speed PIV) has been established [10]. The adaptable setup with flexible operating modes has already been used for different dual-fuel combustion process investigations [11-14].

2.1. Test facility Flex-OeCoS

Figure 1 shows the working principle of the *Flex-OeCoS* test rig: One cylinder of a motor driven engine block feeds a mixture charge into an optical combustion chamber (Ø60 mm×20 mm), providing maximum optical access through rectangular and round sapphire windows at each side. Two intake valves (Ø16 mm) are located on the working cylinder, which is equipped with a flat-top piston. Two exhaust valves (Ø16 mm) are positioned on top of the combustion chamber, where a central bore at the top allows mounting of a pilot fuel injector, spark plug or pre-chamber. Various pressure sensors are implemented at different locations, and the entire head is thermally conditioned to achieve stable conditions during the aperiodic operation.

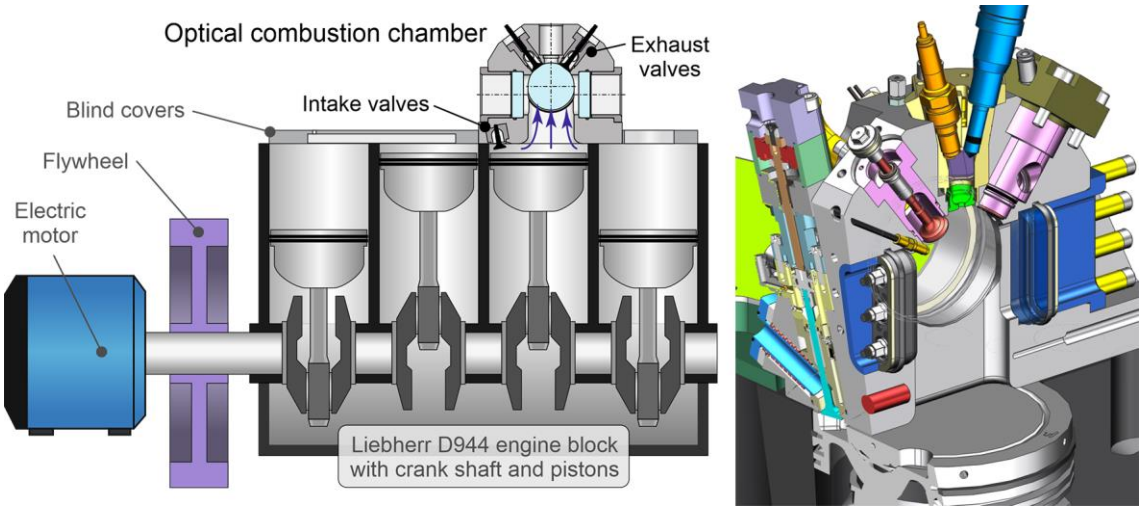

Figure 1: Concept of the Flex-OeCoS test facility (left), and cylinder head on the working cylinder with optical combustion chamber, intake/exhaust valves, and exchangeable design for different inserts on top (right). The optical accessible pre-chamber (yellow) is installed from the top between the exhaust valves (red) and features a sparkplug (orange), a direct injector (blue), a pressures sensor and an exchangeable nozzle (green).

The *Flex-OeCoS* test facility features adaptable operation at IC engine relevant conditions: Peak pressures in continuous operation of up to 260 bar (from boost-adjustable compression pressure (p_c) up to 160 bar), mixture charge temperatures (T) between 700 – 1050 K by inlet conditioning, and tunable flow (turbulence grades) depending on motor speed (n) of typically 300 – 1000 rpm. An overview of relevant test facility specifications is given in Table 1.

Table 1: Test facility specifications and parameter settings

Dimensions, Operating Parameter		
Working cylinder bore	Ø 130	[mm]
Stroke length	150	[mm]
Connecting rod length	237.1	[mm]
Displacement (working cylinder)	1990	[cm^3]
Compression ratio	13.02	[-]
Optical access main chamber diameter	Ø 60	[mm]
Optical access pre-chamber height / width	12.5 / 18	[mm]
Max. cylinder pressure	260	[bar]

Reference values (air charge)		
Intake boost pressure p_b	2.65 / 5.8 / 6 / 6.8	[bar]
Compression pressure p_c	70 / 130 / 145 / 160	[bar]
Intake temperature T_{in}	100 / 150	[°C]
Motor speed n	600	[rpm]
Turbulence intensity u'/C_m [9]	1.2	[-]

Independent pneumatic intake and exhaust valve actuators provide high variability. Moreover, pilot fuel injection settings (pressure, start, and duration) as well as mixture charge composition, by gas introduction in the air intake pipe close to the intake valve, can be freely adjusted by external supply units.

2.2. Optical setup, methodology and post-processing

As illustrated in Figure 2, simultaneous high-speed Schlieren/OH* chemiluminescence was applied to investigate prechamber combustion, combustion transition, ignition processes, turbulent flame front propagation, and abnormal combustion characteristics. Image acquisition was performed by means of three high-speed cameras: The chemiluminescence of the OH* radical as indicator of inflammation was acquired simultaneously with the Schlieren signal indicating vaporized and burned phases within the main chamber. A third Schlieren setup is focused on the optically accessible prechamber delivering insight into the ignition process around the sparkplug and flame evolution. The spatial resolution has been set to 60×60 mm (covering the entire main chamber) and 12.5x18 mm for the pre-chamber to achieve a temporal resolution of 0.1°CA, for the typical motor speed of n = 600 rpm, resulting in a frame rate of 36 kHz.

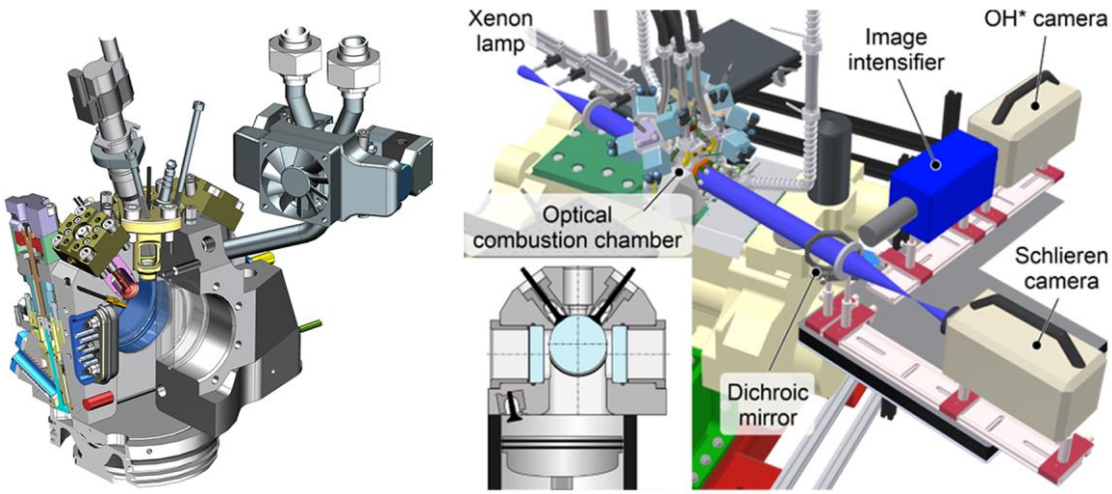

Figure 2: Optically accessible combustion chamber (left) and setup for simultaneous high-speed Schlieren and OH chemiluminescence measurements (right).*

The determination of the effective start of ignition (SOI) is based on the Schlieren signal deviation within the pre-chamber. Due to high turbulence levels, a detection of the flame with a threshold value only often leads to errors. Thus, detection is based on a predefined probability density function dependent on the image zone (background, high-temperature zone, flame) to assign pixel values to a specific location.

The OH* chemiluminescence corresponds to ignition and represents an integrated line-of-sight signal along the entire measurement volume. Even though other species (e.g. CO*), particularly under lean conditions at high pressures, may contribute considerably to the overall OH* signal at progressing combustion [15], the first OH* chemiluminescence emission appears at least simultaneously at ignition [16]. Moreover, also the interference of soot incandescence does not (yet) affect the ignition detection [17], especially since the chosen combustion strategy using pure ammonia should not produce any soot. The start of (high temperature) combustion therefore has been defined as the first OH* appearance, respectively the first image containing a "brighter spot" [18]. The automated optical ignition delay detection proved to be reliable, also compared to the corresponding ignition delay detection from the heat release analysis.

2.3. Exhaust gas extraction, conditioning and measurement

To achieve stable boundary conditions in an experiment, a sufficient number of preparation cycles are run first. This is followed by the actual combustion cycles relevant to the investigation, with further preparation and purge cycles before and after. Due to this process sequence, a fast-switching valve was developed for the exhaust gas analysis, which separates combustion cycles from preparation/purge cycles. Figure 3 shows the corresponding division of the exhaust gas channel by this valve, whereby the combustion cycles to be analyzed are routed into a conditioned system. The entire exhaust path system and sampling line is heated (200 °C) and the exhaust gas storage system has a sufficient volume of 5.1 liters. Moreover, the exhaust gas sampling point distance from the exhaust valve is ca. 500 mm.

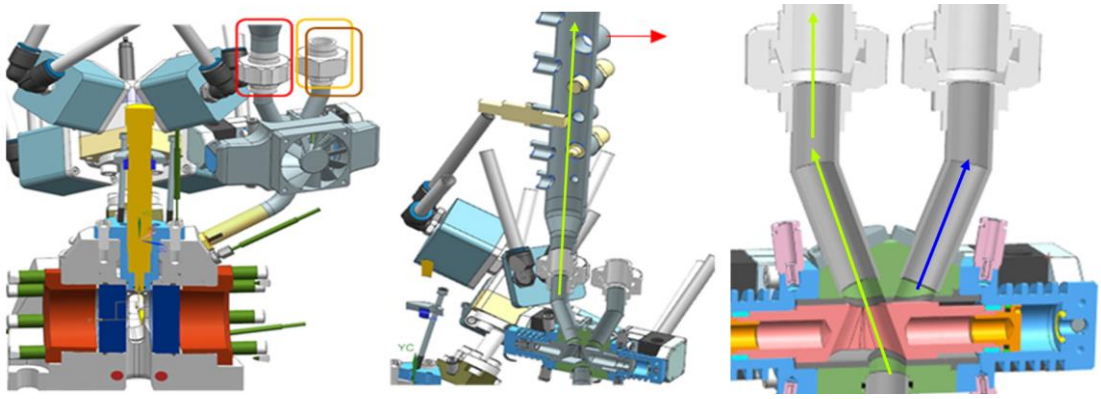

Figure 3: Exhaust gas path separation by a fast-switch valve (left + right), and conditioned exhaust gas sampling section (including sensors) in front of the exhaust gas storage system (center) with marked sampling point (red arrow).

The exhaust gases are then analyzed using a FTIR based measurement system (AVL SESAM i60 FT SII), which is equipped with a special evaluation method for ammonia combustion granting fast and exact exhaust gas evaluation in a wide range of NH_3 concentrations (up to 30'000 ppm NH_3 calibrated) and simultaneous detection of other species. The test bench is now capable to produce appropriate exhaust conditions, similar to those in a single-cylinder engine. It should be noted that the optical setup has an increased crevice volume which causes the exhaust gas composition regarding unburned fuel to be overestimated. The flexible combustion process variation and rapid fuel switching possibilities also allows efficient and comprehensive examinations of various exhaust gas measurement techniques.

2.4. Measurement procedure and analysis

The settings in Table 2 compression temperature (T_c), compression pressures (p_c) are based on pure air compression. These are denoted as reference values for all gas/air combustion investigations, where certain parameters, such as effective compression pressure and temperature, are dependent on the specific gas respectively mixture charge properties.

Table 2 gives an overview of performed measurements operation settings in terms of ammonia/air or methane/air mixture charge conditions such as air-fuel equivalence ratio (λ) and boost pressure variation. Gas admission pressure, start and duration (based on initially determined injection rate characteristics according to energizing time) can be set independently by a separate fuel supply unit to accommodate the boost pressure variation.

Table 2: Measurement conditions and pilot fuel injection parameter settings.

NH_3/air mixture charge		
Air-fuel equivalence ratio λ_{NH3}	2.0 / 1.75 / 1.5 / 1.25 / 1.0	
Start of gas admission	60 °CA before intake valve opens	[°CA]
Pre-chamber fuel	NH_3 ~ λ=1	[-]
Compression pressure p_c	*setting dependent* → see results	[bar]
Compression temperature T_c	*950*	[K]

Pre-chamber parameters		
Pre-chamber Injector	VDO 1353	
Pre-chamber Volume	3.49 / 2.1	[ml / %]
Nozzle diameter d_{nozzle}	Ø 4	[mm]
Start of ignition *SOI*	−10 / −7.5	[°CA]
Spark gap	0.25	[mm]
Coil load time *ET*	5.1	[ms]

Start of ignition, ignition delay (location), combustion onset, and flame propagation have been evaluated by post-processing procedures of the simultaneous high-speed Schlieren and OH* chemiluminescence measurements as well as the exhaust gas measurements. Combustion heat release rate has been analyzed by applying an in-house thermodynamic two-zone model that considers dissociation in the

burnt gas zone and accounts for losses by wall heat transfer, piston ring blow-by, and crevice volumes [19]. Due to the unique test facility layout (optical combustion chamber vs. working cylinder), significant efforts were made in terms of high precision pressure acquisition [10]. The wall heat losses were estimated using an adapted Woschni approach (inclusive extended heat transfer coefficient α_W based on flow measurements), piston-ring blow-by was measured, and the volume of crevices was determined from the drawings. However, since the wall-heat loss model had to be tuned by distinctive constants, the results are denoted as apparent heat release rate aHRR.

The ignition delay can be deduced from both optical data (OH* chemiluminescence) and from the calculated heat release rates. The heat release rate based ignition detection is well tuned and shows a very good agreement with the optical data (already presented in [318]). The ignition delay calculation method is very sensitive and therefore allows to detect ignition at about 0.35% - 0.5% of the total heat released.

An apparent flame propagation speed s_{aFP} can be determined by the Schlieren measurements, respectively the contour displacement representing the flame surface. The method applied here consists of a two-dimensional spatially averaged evaluation of reaction zone expansion based on the optical measurements. It resolves local behavior very well (i.e. large propagation speeds) but is also more prone to misidentification of burned zones since it still contains certain uncertainty in differentiation of the cause of refractive index variations. In addition, the effect of flame compression and expansion cannot be corrected for pressure variations, and the determined s_{aFP} always includes the effect of the expanding burned zone. Thus, higher pressure ratios are affecting the resulting s_{aFP} stronger for lower air-fuel equivalence ratios. However, the chosen approach can deal with (local) transport phenomena and leads to an accurate statement in terms of the early combustion phase. The designation "apparent" shall point out that the analyzed flame propagation speed must be interpreted as a qualitative value that nevertheless enables a comparison within operating parameter variations.

The properties of ammonia as fuel are compared to methane as standard fuel in Table 3 for visualization of the large discrepancies in terms of AFR, LHV and flame speed. The low flame speed of ammonia results in a slower combustion process, which can reduce the combustion efficiency. The high auto-ignition temperature and enormous heat of vaporization makes liquid injection and diesel-like compression ignition combustion more difficult – this is one of the reasons why a premixed combustion scheme is used. The high minimum ignition energy means that it is comparably more difficult to safely ignite an ammonia-air mixture. The high resistance to knocking (RON) allows to run ammonia fueled engines at higher compression ratios, which can be beneficial for efficiency. This should allow to run high IMEP despite the low reactivity by applying high compression temperatures, which results in a high specific cylinder load. Although ammonia has a much lower energy content per mass than carbon-based standard fuels, its low stoichiometric air-fuel ratio AFR partly compensates this regarding the in-cylinder energy content.

Table 3: Properties of ammonia and methane. Data collected for comparison only from [22-26].

	Storage conditions	Density @ storage conditions [kg/m³]	LHV @ storage conditions	Flammability limits in air [Vol-%]	Stoichiometric AFR (mass) [-]	LHV per Vol. @ stoichiometry (0.1 MPa, 373 K) [MJ/m³]	Auto-ignition temperature [K]	Minimum ignition energy [mJ]	Heat of vaporization [kJ/kg]	LBV @ stoichiometry (0.1 MPa, 300 K) [m/s]	RON [-]
Ammonia NH_3 (Liquid)	1.1 MPa 300 K	600	18.8 MJ/kg 11.3 GJ/m³	15 – 28	6.1 : 1	~ 2.23	930	8	1370	0.07	> 130
Methane CH_4 (Compressed)	25 MPa 300 K	187	50 MJ/kg 9.4 GJ/m³	5 – 15	17.2 : 1	~ 2.45	860	~ 0.21	–	0.38	120

3. Results

The results shown here are from a large measurement campaign and represent only a subset of all the measurement points carried out. They provide an insight into pure ammonia combustion using a pre-chamber in terms of pressure evolution, ignition delay, combustion onset, flame propagation, heat release and exhaust gas composition.

3.1. Combustion characterization varying the air-fuel equivalence ratio

Figure 4 shows a comparison of the pressure development for two different boost pressure levels consisting of an ammonia charge mixture variation with air-fuel equivalence ratio λ = 1.0 / 1.25 / 1.5 / 1.75 (/ 2.0) / inf. The spark timing within the prechamber is set to -10° CA corresponding to a pure air compression temperature of about 950 +/-5 K[14], [21], for both cases. Keeping the compression temperature nearly constant over a boost pressure variation is possible since the charge air is entering a separately pre-heated intake pipe to achieve individual pressure and temperature combinations. The pressure trace represents the median cycle value of fifteen combustion cycles and additionally the pressure trace of the pure air compression (idle, i.e. motored) is given in dashed line. The difference in pressure evolution between the two boost pressure levels is visible in two terms. Firstly, in maximum combustion pressure level, achieving 150 bar for the 70 bar compression pressure versus 280 bar for the 130 bar compression level regarding λ = 1.0 (and therefore exceeding the maximum allowed continuous operating pressure), secondly in terms of pressure gradient. The 70 bar compression level case thereby shows a decreasing pressure gradient with increasing λ, whereas in the high boost case the pressure gradient for λ = 1.0 to 1.5 remains nearly constant. For the low boost case, it is observable that the λ = 2.0 case has barely an increase in compression pressure, leading to the assumption that there is a high portion of unburned fuel exiting the combustion chamber.

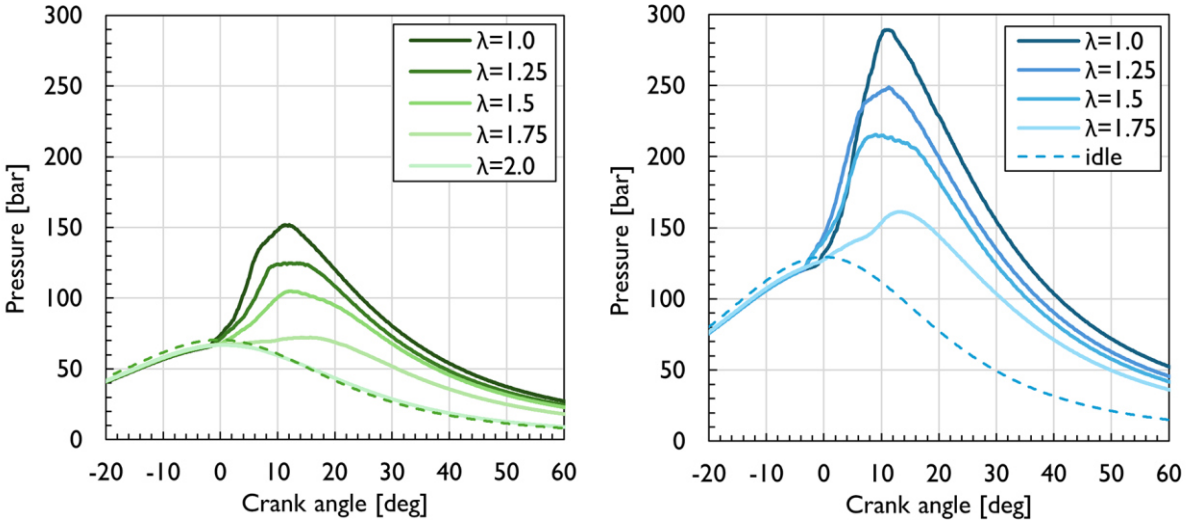

Figure 4: Comparison of the pressure development for two different boost pressures resulting in 70 bar (left) vs. 130 bar (right) compression pressure and a variation of λ. For the λ = 1.0 case at 130 bar, the SOI had to be retarded from -10 to -7.5° CA to avoid knocking.

The higher cylinder pressure at 130 bar compression pressure is on the one hand coupled to the already increased pressure before ignition, but on the other hand due to the increased air density allowing more fuel to be admitted to reach comparable air-fuel-equivalence ratios. Hence for the λ = 1.0 case for 70 bar 571 mg fuel was injected per cycle compared to 904 mg fuel for the 130 bar compression pressure case. Therefore, an increase of 58% in in-cylinder energy content can be expected. This increase in fuel energy is easily observable when comparing the heat release rate for both cases. Additionally, to the heat release rate the mass fraction burned is given for both cases and is represented in Figure 5. The heat release rate thereby represents the already observed discrepancy between the 70 bar case versus the 130 bar compression pressure, whereas the heat release increase in the early combustion phase is quite similar for λ = 1.0 to 1.5 for the 130 bar case. The main influence hereby is the higher integrated heat release before TDC, increasing the in-cylinder temperature before TDC and therefore stabilizes or even promotes the reaction rate for the leaner cases. This results in high combustion temperatures which allows the fuel oxidation in the phase after TDC to an acceptable level. This absolute fuel conversion level is then represented in terms of mass burned fuel fraction. The mass fraction burned is calculated based on the injected fuel mass and supported by the exhaust analysis giving the unburned fuel mass and side reactions which will be later represented in chapter 3.3. The high fuel conversion rates for the 130 bar case between 98.9% and 99.0% for the λ = 1.0 to 1.5 (98.7% for the λ = 1.75) cannot be reproduced at lower compression pressures. As already mentioned, the test-bench has large crevice volumes of about 1% of the TDC volume. Therefore, a fuel conversion rate of 99% represents nearly complete conversion in premixed cases.

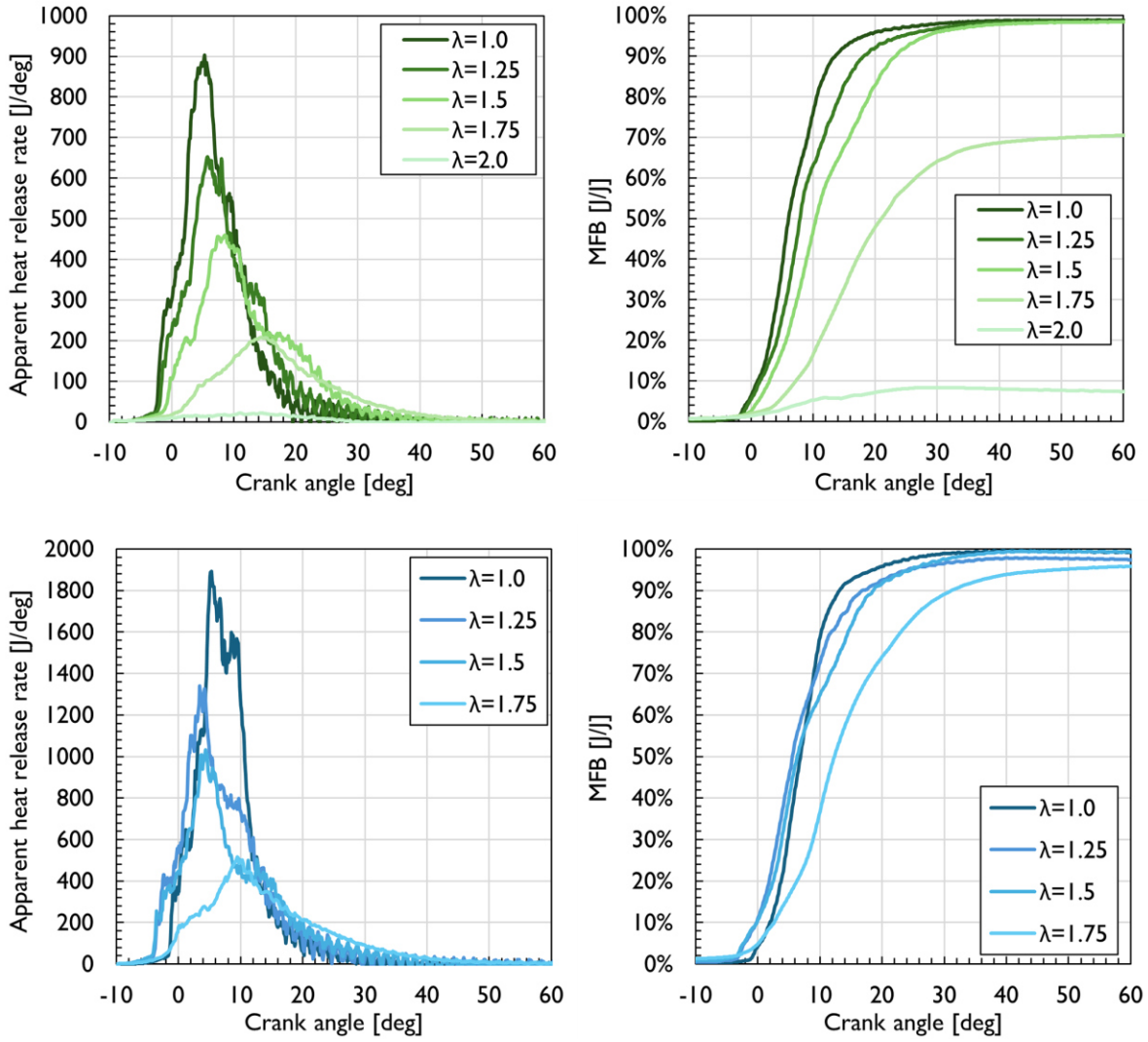

Figure 5: Apparent heat release rate (left) for 70 bar (top) and 130 bar (bottom) as well as mass fraction burned for both cases. All plots represent air-fuel-equivalence ratios between λ = 1.0 and λ = 1.75 (2.0). For the λ = 1.0 case at 130 bar, the SOI had to be retarded from -10 to -7.5° CA to avoid knocking.

The fuel conversion rates are in terms of mass fraction burned at 70 bar compression pressure is dropping earlier and faster to very low levels of 70% for λ = 1.75 resp. below 10% for λ = 2.0. Since these low fuel conversion rates are not acceptable in terms of fuel and cost effectiveness and emissions, such high air-fuel equivalence rates are only possible for full load operation of an engine at maximum boost pressure and compression temperature.

The optically accessible test bench has the benefit of an observable combustion process and therefore both Schlieren images and the superimposed OH* chemiluminscence images for the mainchamber are shown in Figure 6. These image series allow to evaluate the earlier stated assumptions based on the pressure signal acquisition. Wheras the pre-chamber is operated at nearly constant air-fuel equivalence ratio due to its separate ammonia injector (resulting in comparable ignition delays in the pre-chamber), the main chamber represents a λ-variation between λ = 1.0 to λ = 1.75 for 130 bar. The hot reactive jet enters the main chamber slightly before -1° CA in all cases, whereas the cold jet consisting of non-combusted fuel enriched gases enters the main chamber already around -4° CA. This fuel enriched zone is then ignited first by the hot jet, leading to a comparably higher heat release during flame onset

in the main chamber. This can be observed either in terms of the OH* signal (green) that rapidly increases between -1° CA and 0° CA, or in the Schlieren signal that shows a rapidly increasing surface area within the black border. The subsequent reaction rate can also be observed in terms of OH* chemiluminescence (green overlay intensity): Whereas the fuel rich cases show a strong color, the lean cases only show a relatively low OH* chemiluminescence intensity, leading to the assumption that the heat release rate must be low as well, which is confirmed by Figure 5.

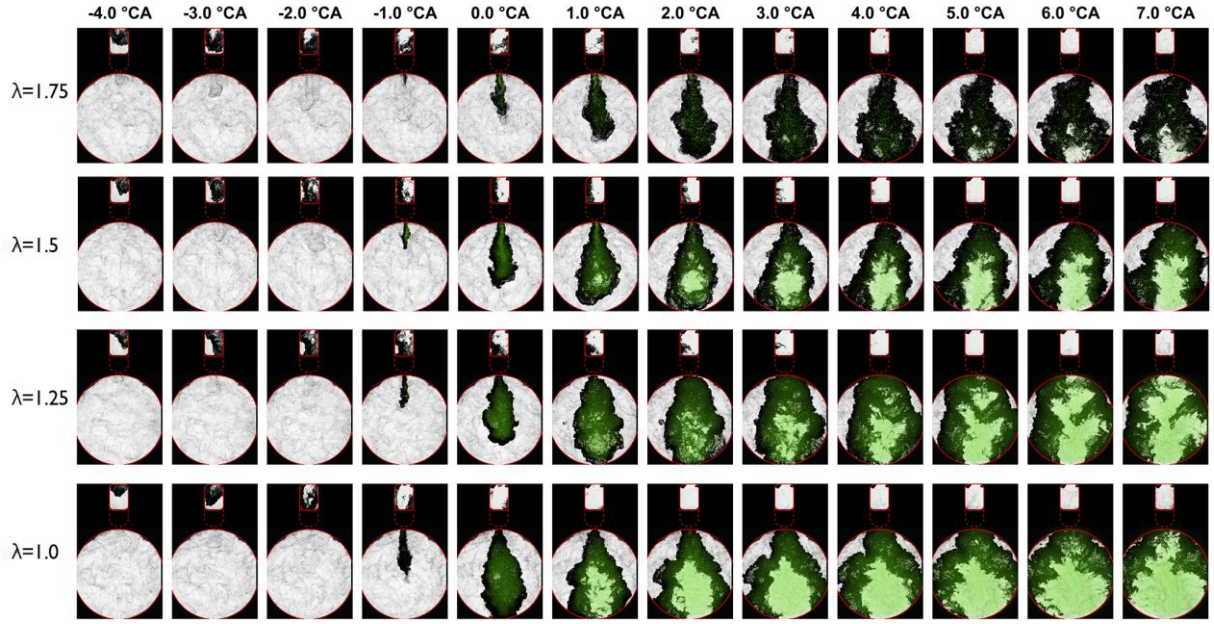

Figure 6: Image series with different air-fuel mixtures from λ = 1.0 to λ = 1.75 at 130 bar compression pressure and SOI = -10° CA showing superimposed high-speed OH-chemiluminescence and Schlieren images for both main and pre-chamber. The λ = 1.0 case shown here is a non-retarded cycle and features an SOI = -10° CA as well. Here pre-ignition can be observed at top left, knocking occurred later in the non-observable area.*

The directly observable phenomena were further evaluated using an in-house tool to calculate apparent flame speed s_{aFP} for both pre- and main chamber. Whereas the stoichiometric conditions within the pre-chamber are constant due to an increasing addition of NH_3 for the leaner cases, a variation in flame speed within the pre-chamber is nonetheless observable, especially for the two leaner cases. A lower flame speed is connected to either leaner or richer conditions than λ = 1.0, since the flame maximum speed must be near λ = 0.97 [28].

Since the air-fuel equivalence ratio in the pre-chamber cannot be measured directly, an alternative procedure was chosen to achieve stoichiometric conditions. Thereby, the energizing time (ET) of the pre-chamber injector was chosen iteratively by varying the ET until the highest possible flame speed with the lowest cyclic fluctuations (corresponding with λ = 1.0) was achieved. This was double checked using the static fuel flow rate for the pre-chamber injector and the theoretical fresh charge fill volume. The inflow of fresh charge leading to dilution is a factor that could not be fully considered within this project since detailed LES-Simulations would be needed to address this problem. For the lean cases, the fuel admission must be started very early (near BDC) and hence fuel loss out of the nozzle adds an additional uncertainty that results in a residual variation of λ within the pre-chamber. These two effects are more pronounced for the lean cases since escaped fuel, or entrained air, have a huge impact on the stoichiometry. The s_{aFP} within the main chamber then shows the typical decreasing flame speed for leaner cases, which can be expected for ammonia as well as methane and other fuels [20]. The fuel-

richer cases are showing a very high gradient in flame speed increase during flame onset within the main chamber. This can be seen in Figure 6 as well, where the flame front is propagating not only from top to bottom in front of the reactive jet, but also from the center towards the left and right side along the entrained jet, leading to a very large flame front and hence to a high flame front growth rate, resulting in the high gradient in s_{aFP}. At 130 bar compression pressure, the $\lambda = 1.0$ case shows a much lower flame speed (comparable to $\lambda = 1.75$ at 70 bar compression pressure) and a lower gradient. For this case the SOI within the pre-chamber had to be retarded from -10 to -7.5° CA to avoid knocking. The slower flame front increase is based on two main factors: the cylinder pressure and the turbulence level. Whereas the higher cylinder pressure leads to lower flame speeds, the turbulence level inside the main chamber drops as well, especially near TDC [9]. The start of jet entrainment is then further retarded due to a simultaneous drop in turbulence level within the pre-chamber. This effect is very pronounced towards TDC and already described in [20]. In Figure 7 bottom, left it is observable that the flame speed instantly increases after the spark at -10° CA for the corresponding cases, whereas the SOI of -7.5° CA leads to a slightly delayed increase in flame speed of around one degree since the already dropping turbulence reduces the reaction rate. In Figure 6 a non-retarded cycle of $\lambda = 1.0$ is compared with the other air-fuel equivalence ratios at 130 bar where it can be observed that the flame speed does not decrease to fuel leaner cases, rather it further increases, since the full burned zone reaches the walls earlier. This substantial higher flame speed within the main chamber is on the one hand coupled to the turbulence level before the jet penetration, and on the other hand coupled to the additional turbulence from the entraining reactive jet. The high velocity brings in a lot of turbulence and increases mixing and re-entrainment leading to elevated reaction rates.

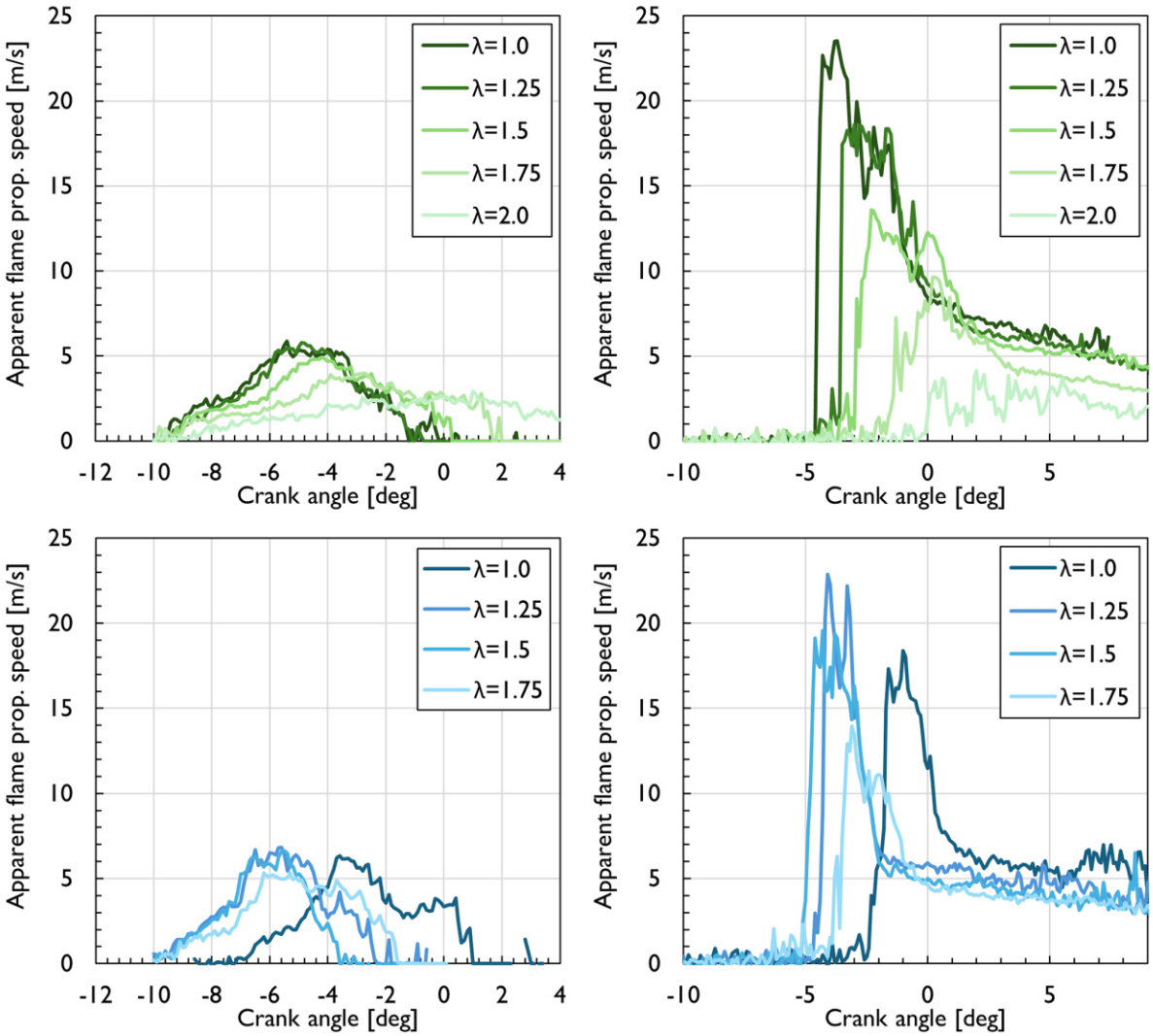

Figure 7: Apparent flame speed (s_{aFP}) based on high-speed Schlieren measurements for the pre-chamber (left) and main chamber (right) for two different boost pressures leading to a compression pressure of 70 bar (top) and 130 bar (bottom). For the case with λ = 1.0 at a compression pressure of 130 bar, the SOI had to be retarded from -10 to -7.5° CA to avoid knocking.

The differentiation between flame speed within the combustion chamber and effective heat release (resulting in an increasing cylinder pressure) is very important. Figure 8 shows the apparent flame speed on the y- axis vs. the apparent heat release rate on the x-axis and attempts to clarify this. If there would be a linear dependency, all the points would be on a diagonal from the bottom-left to the top-right corner. Nevertheless, the diagram shows another dependency: whereas the flame speed increases during the initial phase, the heat release rate does not increase in the same manner. In the beginning, the high flame speed due to jet turbulence is only present for a small proportion of the overall area. Therefore, the flame speed must be combined with the flame surface area to get a direct link to the

expected heat release rate. It is also very important to consider the combustion chamber shape as well as the position and number of the reactive jets from the pre-chamber to compare these results.

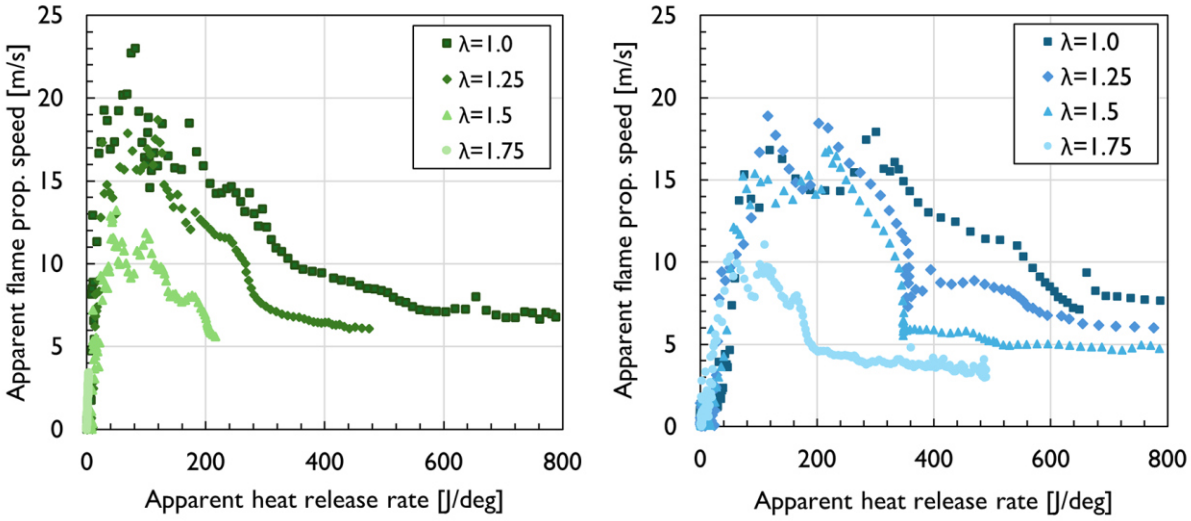

Figure 8: The apparent flame propagation speed in the main chamber vs. the apparent heat release rate shows the dependency between flame propagation and effective heat release during flame onset and initial flame propagation.

When looking at the 130 bar case for λ = 1.0 (Figure 8, right), three phases can be described. The first phase from 0 J/deg to 350 J/deg, the second phase from 350 J/deg to 460 J/deg and the third phase from 460 J/deg to the end. In the first phase, the initial flame front is initiated by the reactive jet (flame onset in the main chamber) and rapidly increases in size, then the flame speed remains at a certain level. The second phase is dominated by the flame traveling deeper in the combustion chamber, and since the turbulence level decreases around TDC, the flame speed decreases further. The third phase shows a second large decrease in flame speed. This happens when the reaction zones hit the walls, where the flame speed drops to zero, and the flame can only travel towards the remaining unburned zones. The end of the combustion cannot be observed within the optical accessible area due to the combustion chamber shape.

3.2. IMEP-variation by different cylinder charge conditions

In this section, results from an intake pressure variation, similar to a load variation in a real engine, are presented. The intake pressure influences both compression and combustion pressure and hence results in different IMEP and output power of the test bench. In addition to the pressure variation itself, a λ variation is also performed within the operating limits of the test bench.

In Figure 9 (left) cylinder pressure traces of a IMEP variation are shown at a constant λ for two high load points at IMEP = 26 bar and 20 bar, whereas a part load point with IMEP = 10 bar is shown as a comparison. All operating points have a similar compression end temperature and feature the same start of ignition at -10° CA. The high load point with 26 bar IMEP slightly exceeds the design pressure of the test bench (260 bar) but is still below the safety limit of 330 bar when the cylinder head lifts off due to the overpressure. Since the operation was very stable without any pre-ignition and abnormal combustion behavior, this high IMEP dataset has been considered as well.

The corresponding pre-chamber pressure and the difference between pre-chamber and main chamber pressure is illustrated in Figure 9 on the right. The pressure difference between pre-chamber and main

chamber is targeted to be in the range of 10 and 20 bar for full load – a 4 mm single hole was found to be suitable for all experiments carried out. Whereas the high load points have a similar maximum pressure difference in the order of 16 to 17 bar, the part load operation would benefit from a smaller nozzle size to reach the same pressure differences. The pressure difference between pre-chamber and main chamber is the main driver for the penetration length of the reactive jet and therefore important for increasing the turbulence within the main chamber.

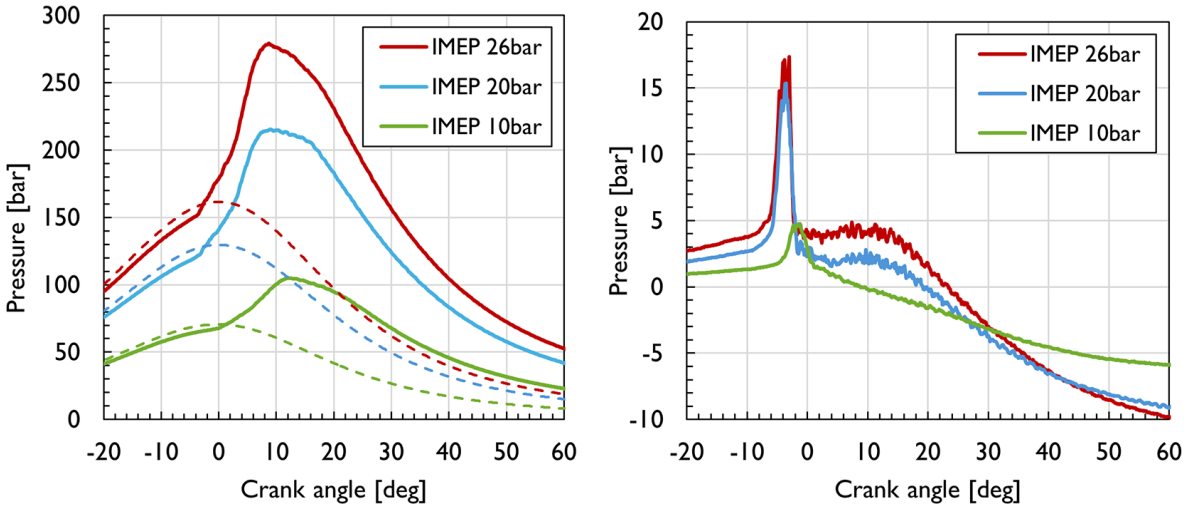

Figure 9: Left: cylinder pressure traces for three different IMEP at constant λ (λ = 1.5) including the idle cycle (dotted line). Right: pressure difference from pre-chamber to main chamber for those operating points.

The heat release rate for the 20 bar and the 26 bar IMEP load points are very similar in shape – only the level is slightly higher for the higher IMEP. This leads to a nearly identical shape of the mass fraction burned in Figure 10 (right). The fuel conversion rate is very high and in the range of 98.7 to 99.0% for all three experiments. The part load operating point with IMEP = 10 bar shows a slightly slower increase in heat release rate. The main reason is the reduced energy density, which results in colder in cylinder conditions during combustion and hence a reduced reaction rate. In addition, a smaller absolute heat release rate must be expected anyway since only about half the amount of fuel is contained in the cylinder at this load point. If the integrated heat release rate is normalized with the total fuel energy, then the result is quite comparable to the high load points – only a slight shift towards later crank angles can be observed.

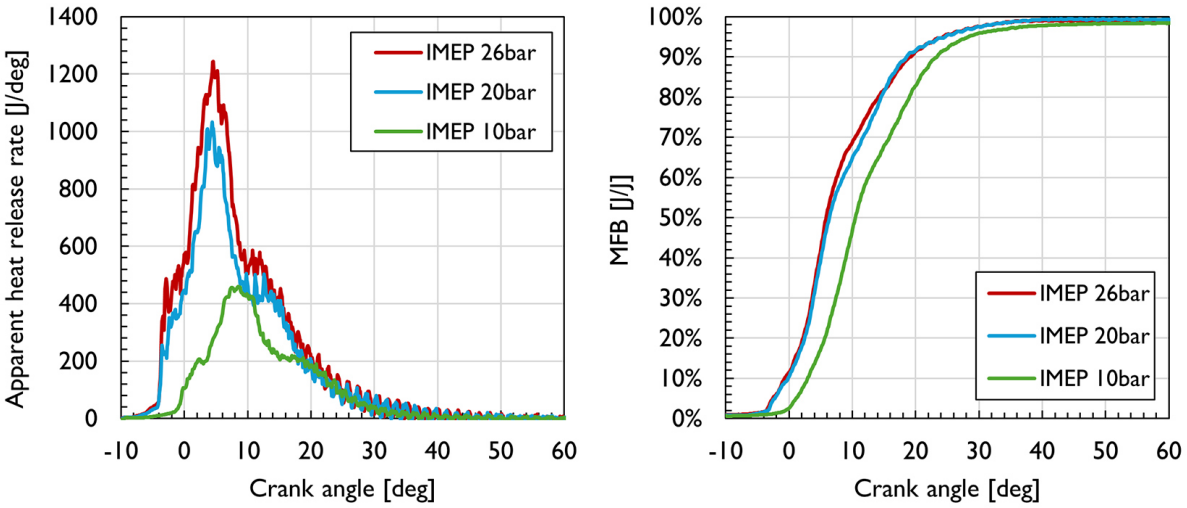

Figure 10: Heat release rate (left) and mass fraction burned (right) for three different IMEP at λ = 1.5.

In addition to the three already shown data sets for a constant λ of 1.5, the measurement matrix was extended to include a wider variation of boost pressures and λ. The results are summarized in characteristic combustion numbers in Figure 11 and Figure 12. The additional measurements resulted in IMEP between 5 bar and 30 bar (which is the highest IMEP achieved so far in the test bench). For each boost / compression pressure, λ was increased as long as the fuel conversion rate remained high (as discussed in 3.1). Consequently, at the λ resp. fuel conversion limit, a slightly decreased IMEP is observable for a compression pressure of 70 bar above λ = 1.5 and for 130 bar above λ = 1.7.

The ignition delay shown on the right side of Figure 11 is an important characteristic number for designing the combustion process in an engine and therefore important to know for different fuel-air ratios in the desired load range. The ignition delay shown here is the delay between start of discharge of the spark plug in the pre-chamber and start of combustion in the main chamber (i.e. a certain level of the heat release rate). The presented ignition delay for the higher load cases of around 1.2 ms is quite low for such a coupled combustion chamber, especially since pure ammonia is used as fuel. The nearly constant ignition delay behavior in a wide range of air-fuel equivalence ratios for the 130 bar case is beneficial for the combustion control strategy. When running part load, the ignition delay increases drastically and therefore would need additional measurement points to fully characterize this load regime. Otherwise, the spark discharge timing can be delayed to achieve full combustion resp. to get the desired torque. The highest boost pressure setpoints, leading to a compression pressure of 160 bar, have ignition delays below 1 ms. But, as already shown earlier, the ignition delay for the pre-chamber configuration is very sensitive regarding the chosen the spark discharge timing due to its strong dependence on the (decreasing) turbulence level around TDC.

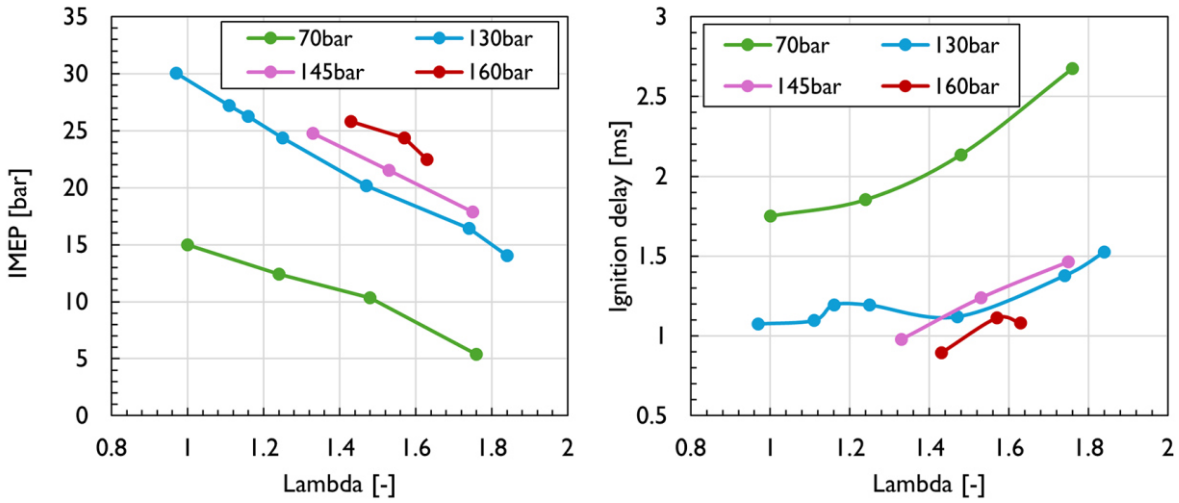

Figure 11: IMEP (left) and ignition delay of the main chamber charge (right) for a λ-variation at constant boost resp. compression pressure.

Figure 12 illustrates the stochastic phenomena of this type of combustion. Where diesel-like combustion schemes benefit from a very low coefficient of variation (COV), pure Otto-Cycles are well known to deliver higher COV. For pilot ignited dual-fuel combustion the COV mainly depends on the pilot fuel amount, which stabilizes the main combustion. Since the pre-chamber ignited combustion scheme is a combination of a spark plug initiated combustion followed by a reactive jet ignition it can be expected that it results in higher COV. For the $\lambda = 1.0$ case regarding 70 bar and 130 bar compression pressure, the COV is quite low at 1% resp. 2.5%. In general, for the 70 bar case the COV remains at very low values of around 2% which is very good for this type of combustion scheme, especially for ammonia combustion. Higher boost pressures lead to higher COV since the local transport phenomena have more influence within the main chamber. For the highest boost pressure of 160 bar, abnormal combustion behavior with pre-ignition further increases the COV. The plot in the center of Figure 12 represents the knock intensity (KRAT) according to Siemens-VDO (which is used in AVL indicating systems as well), where knock intensities above two are interpreted as knocking cycles. The knock intensities for all cases are non-critical, but nonetheless need certain attention. Leaner cases also show relatively high knock intensities, which is not expected. This is due to pressure fluctuations within the coupled combustion chambers that form a mass-spring oscillating system, which results in pressure oscillations even without knocking. Therefore, an in-house approach specifically designed for this test bench is used to evaluate the real knocking influence including min and max levels of all cycles and is shown in the plot on the right side of the Figure 12.

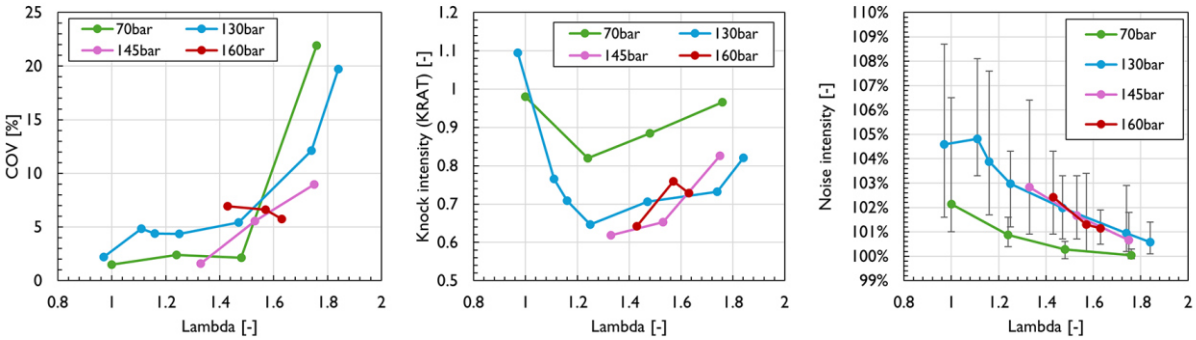

Figure 12: COV (left), knock intensity according to Siemens-VDO algorithm (center) and noise intensity according to the FHNW algorithm (right).

This so-called "noise intensity" calculates the intensity of stochastic noise above the normal noise level within the pre-chamber based on the pressure measurement. A reference window is used to characterize the amplitude of a pressure fluctuation from a non-knocking window, which is then compared to a pressure fluctuating coming from a higher-pressure gradient than during the initial flame propagation. This algorithm is very sensitive to knocking or hard combustion. A level of 100 % means that the combustion related pressure fluctuations correspond to a normal combustion. This algorithm shows the expected trend where fuel-air mixtures towards stoichiometric conditions should deliver the highest knock intensity levels. The maximum levels of the noise intensity was calculated to be 9% over standard pressure oscillation levels, leading to the assumption that only a very small share of the total fuel amount could have been combusted in a knocking manner.

3.3. Emission characterization for a wide range of IMEP

The emission characterization is an important task for all engine manufacturers to comply with current emission regulations. Since ammonia engines are intended to reduce the CO_2 based GHG emissions, it is very important to reduce nitrous oxide (N_2O) emissions to an absolute minimum level, since its GHG factor is nearly 300 times that of CO_2. Because ammonia contains nitrogen in its molecular structure, NO_x emissions are expected to be high as well. For an in-cylinder reduction of NO_x, a stoichiometric or even slightly rich combustion can probably reduce NO_x drastically since it provides a nearly identical pathway to reduce NO_x as in an SCR after treatment system using urea. The emission measurements are shown in Figure 13.

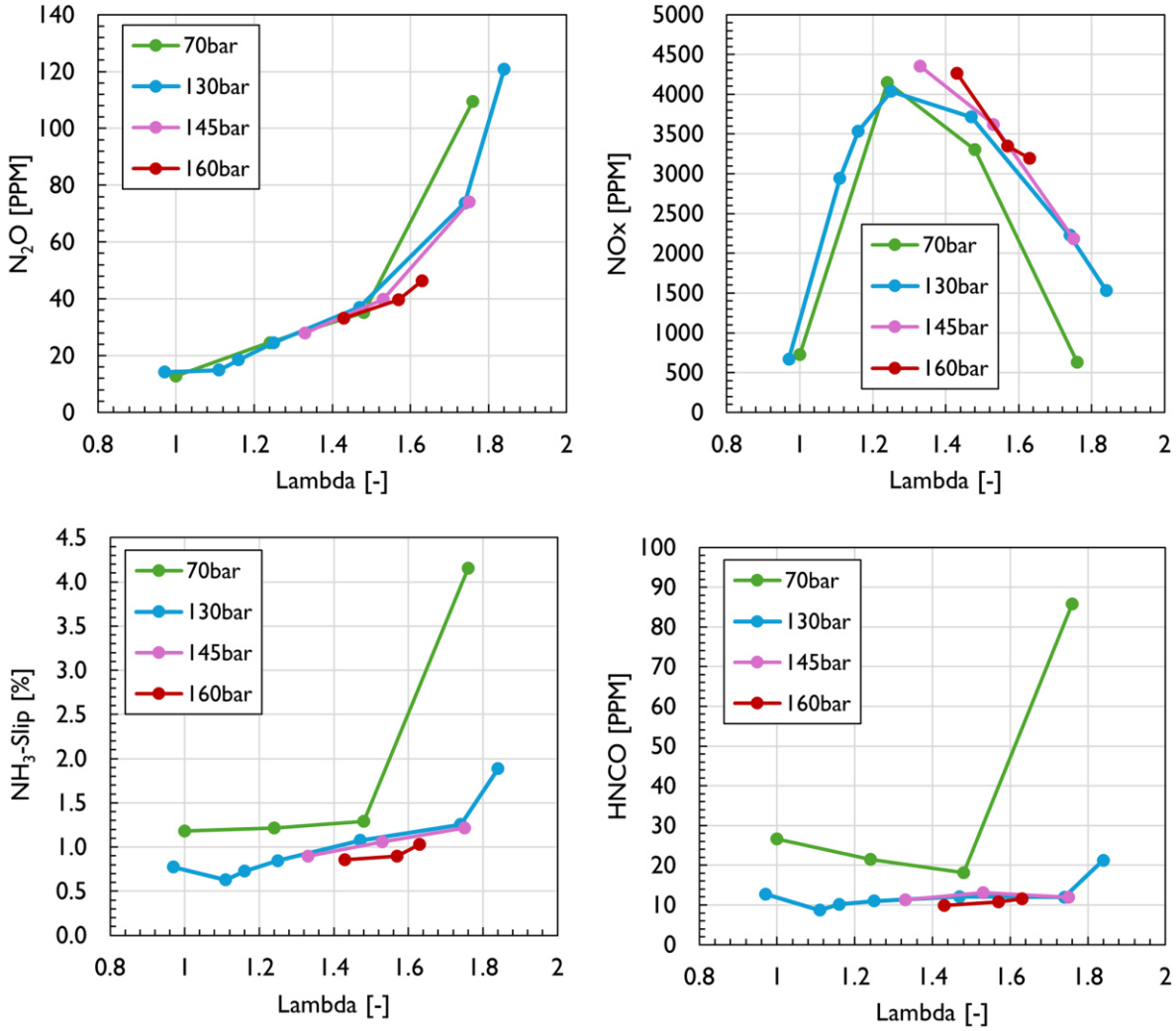

Figure 13: Emission characterization for all presented measurements with a λ-variation at different boost resp. compression pressures.

The measured N_2O levels are largely independent of the load point but depend on the fuel-air ratio. They are also very sensitive regarding incomplete combustion. To achieve low engine-out N_2O emissions therefore the engine should be designed to run at stoichiometric conditions, which is also favorable in terms of NO_x emissions as well. The maximum NO_x peak can be observed around $\lambda = 1.2$ for the different boost pressures – comparably low emission levels can only be achieved when the engine runs around $\lambda = 2.0$. However, such high air-fuel equivalence ratios can be problematic regarding the fuel conversion ratio as shown in the previous section. The NH_3-Slip, measured with the FTIR, supports this as well, shown in Figure 13 bottom left. NH_3 emissions are problematic due to its toxicity, in addition even very low concentrations far below the tolerable exposure limits can be detected by the human nose. Futher, NH_3 emissions directly increase the operating costs of the engine. Figure 13 bottom right represents the isocyanic acid (HNCO) emissions coming from the ammonia reacting with CO_2. HNCO has been identified as a concern for human health and therefore gains certain attention. The levels for the full load cases are generally very low. The high value of nearly 90 ppm for the 70 bar case at $\lambda = 1.7$ could be some misinterpretation from the FTIR since NH_3 has

exceeded the calibrated range at this point, and a strong interference between HNCO and NH_3 is evident.

Running a commercial heavy duty ammonia engine at $\lambda = 1.0$ is certainly not an easy task. High in cylinder energy contents lead to high mechanical and thermal stress on materials within the engine, and the turbocharging systems must deal with high exhaust gas temperatures. Therefore, the exhaust gas temperature of each cycle has been measured with a 0.25 mm thermocouple in the exhaust to resolve the exhaust gas temperature. The measured mean values as well as the cycle-based min and max values are shown in Figure 14. High exhaust gas temperatures above 500 °C were measured in the near stoichiometric case. Then the temperature drops in function of an increasing λ, nearly independent of the load condition, which is expected since the exhaust gas temperature at constant SOI is mainly influenced by the air-fuel equivalence ratio itself. The plot on the right-hand side in Figure 14 summarizes the dependency between NO_x and N_2O emissions but shows the emissions based on engine power in g/kWh. The best-case scenario for low NO_x and low N_2O emissions is still around $\lambda = 1.0$ or slightly below, whereas $\lambda = 1.6$ results in very high specific NO_x emissions while already increasing the N_2O levels to nearly 0.8 g/kWh.

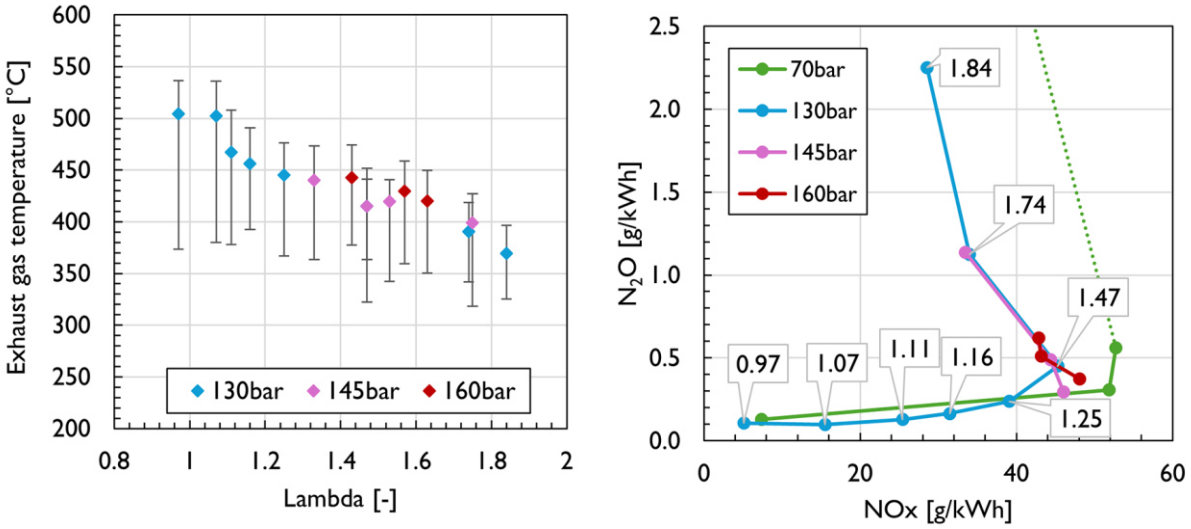

Figure 14: Exhaust gas temperature (left) for all presented measurement points, and the specific engine emissions N_2O versus NO_x for certain air-fuel equivalence ratios (right).

These high levels in specific emissions make a suitable exhaust gas aftertreatment system mandatory. Therefore, several companies are working on new deNO_x and deN_2O SCR-systems to be ready for the new ammonia engine families.

3.4. Abnormal combustion phenomena

In a premixed cylinder charge, the abnormal combustion phenomenon of pre-ignition due to the self-ignition of lubricating oil droplets intruding the combustion chamber and the resulting knocking is often encountered. This type of abnormal combustion phenomenon is characterized in particular by elevated peak combustion pressures, which results in exceptionally high mechanical and thermal loads on components. Another consequence of lubricating oil induced pre-ignition are increased emissions, especially of species exhibiting high temperature dependencies as it is the case with the formation of nitrogen oxides (NO_x).

Figure 15 shows pressure traces (left) of a motored cycle (Idle, dotted line), a normal cycle not affected by pre-ignition at all (Normal, blue line, lower image row) and a cycle affected by lubricating oil induced pre-ignition (Preignition, red line, upper image row).

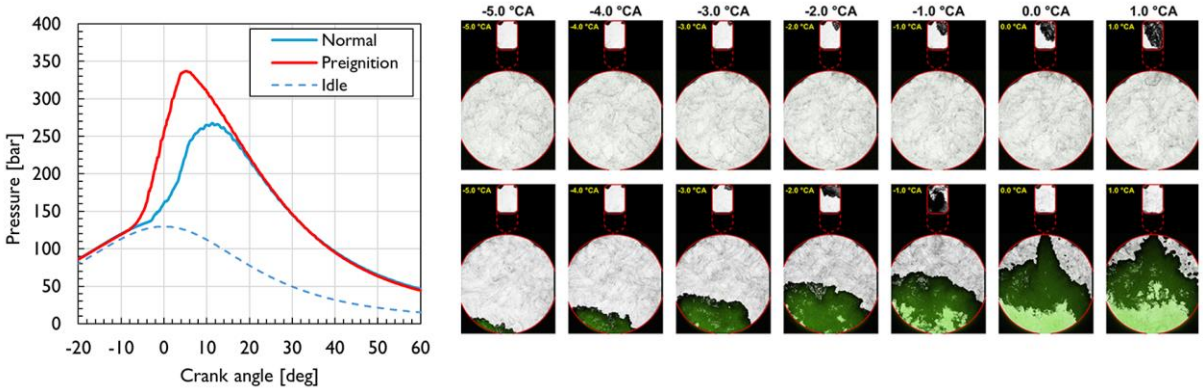

Figure 15: Comparison of pressure development (left) and the corresponding optical measurements (right) for a critical pre-ignited, knocking cycle (bottom images) vs. a normal cycle (top images) for a cylinder charge with λ = 1.0.

From the high-speed Schlieren recordings (right) it can be seen that a flame front originating from the self-ignition of lubricating oil already propagates from the bottom before the actual ignition in the pre-chamber – the reactive jet from the pre-chamber enters the main chamber when a large part of the fuel has already been converted by the pre-ignition. It is well observable that the ignition jet propagates partly through already burnt zones and is consequently disturbed. Later, more flame kernels form in the unburned zone near the combustion chamber wall. Even though more lubricating oil droplets in the combustion chamber could be the source of those additional flame kernels, the already advanced stage of combustion can result in self-ignition of the premixed cylinder charge itself, whereby initial knocking can be indicated based on the multiple ignition locations. During this time, the cumulative flame front surface area and thus fuel conversion increases very fast compared to the normal cycle, which is clearly shown in the elevated pressure rise rate (left). The peak combustion pressure is approx. 25% higher compared to normal cycles (at over 330 bar) due to the 5° CA earlier start of combustion in the case of pre-ignition. Such high combustion pressures can lead to severe damage and even failure of the engine under such operating conditions. Therefore, such pre-ignition events are considered critical and must be avoided.

Figure 16 shows another measurement where the strong influence of the location of pre-ignition in the combustion chamber on the further course of combustion can be seen. The slight shift of the initial flame kernel towards the combustion chamber wall causes the pre-chamber ignition jet to penetrate into a completely unburned zone and thus not showing any interaction with the propagating flame front originating from lubricating oil induced pre-ignition. Due to the over 8° CA earlier pre-ignition initiated start of combustion compared to the time when the ignition jet enters the main chamber, the corresponding pressure trace shows a steeper rise at the beginning. However, due to the high penetration depth and ignition energy of the ignition jet and the associated large initial flame front surface area, regular combustion dominates and is responsible for the main part of fuel conversion. Such pre-ignition events do not overload the engine and are therefore not considered to be critical.

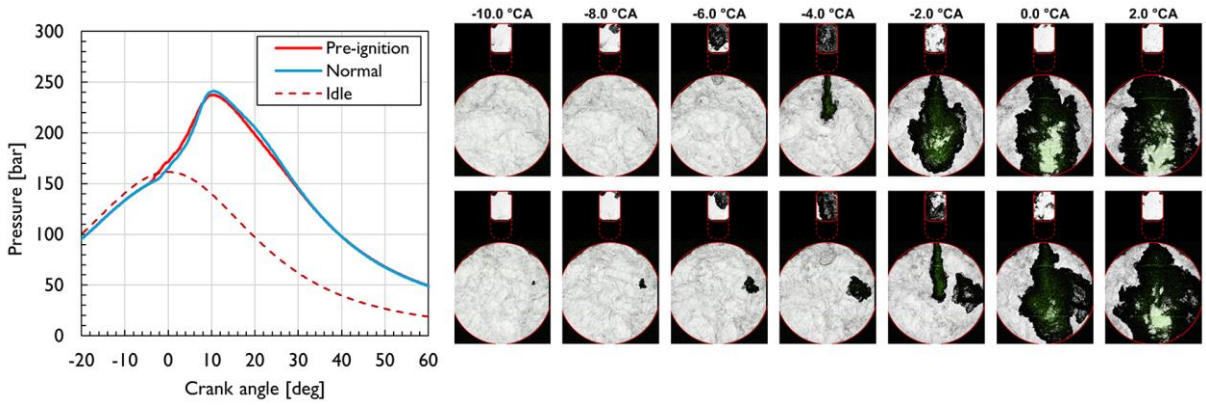

Figure 16: Comparison of the pressure development (left) and optical imaging (right) for a non-critical pre-ignited cycle vs. normal cycle for a cylinder charge with λ = 1.0.

Due to the high fluctuation of the occurrence as well as the influence of the phenomenon on the combustion process, it advantageous to completely suppress rather than minimize lubricating oil induced pre-ignition, especially under such operating conditions.

4. Conclusions

High IMEP combustion of pure ammonia initiated by a reactive jet from a pre-chamber has been successfully carried out in the optically accessible *Flex-OeCoS* test facility for a variation of air-fuel equivalence ratios, boost/compression pressures and loads (IMEP), including a characterization of the corresponding exhaust emissions. The well-known boundary conditions of the test rig allow precise acquisition of pressure and temperature to enable thermodynamic analysis in view of ignition delay, reactive jet transition, heat release, and IC engine characteristic numbers such as mass fraction burned. Moreover, the optical accessibility of the *Flex-OeCoS* test facility allows simultaneous high-speed Schlieren/OH* chemiluminescence recordings of the combustion processes in the pre-chamber and main chamber. Based on these images, an apparent flame propagation speed could be calculated for both the main chamber and the pre-chamber. In addition, qualitative statements could be made about the observed pre-ignition events in the main combustion chamber.

The variation of the air-fuel equivalence ratio between λ = 1.0 and λ = 2.0 gives a deeper insight into the λ-dependent amount of fuel mass burned, which for this combustion scheme is ideal in the range of λ = 1.0 to λ = 1.6 (slightly depending on engine load conditions), while higher loads allow a leaner combustion. Maximum fuel conversion rates of over 99% can be achieved, which is quite high for this particular test bench, which has a crevice volume in the order of 1% of the total combustion chamber volume.

The ignition delay, measured between spark ignition in the pre-chamber and the start of combustion in the main chamber, is between 1.1 and 1.4 ms for a range of air-fuel equivalence ratios at full load (high boost resp. compression pressures), while at part load (low boost resp. compression pressure) longer ignition delays of over 2 ms are observed. The ignition delay is very sensitive to the start of ignition / spark ignition time in the pre-chamber, as it is strongly dependent on the level of turbulence in the pre-chamber, which decays rapidly towards top dead center.

The apparent turbulent flame propagation speed s_{aFP}, calculated from optical high-speed recordings, increases to more than 23 m/s for λ = 1.0 in the early flame propagation phase, which is very high compared to the laminar flame speed of ammonia (~ 0.018 m/s).

The high-speed Schlieren/OH* chemiluminescence images optimally support the classical combustion characterization by pressure measurements and allow a spatially resolved, deeper insight into the ignition and combustion behavior. In addition, abnormal combustion behavior such as pre-ignition, misfiring and knocking can be directly observed and identified, which can be useful for improving engine designs or for the development of combustion models that can predict such behavior.

The accompanying exhaust gas measurement completes the characterization of the ammonia combustion of the pre-chamber initiated combustion process. Nitrous oxide (N_2O), a major pollutant in ammonia engine greenhouse gas emissions, must be closely monitored in the design of new engine families to fully realize the greenhouse gas reduction potential of ammonia engines against a methane burning engine. The N_2O based reduction potential of an ammonia combustion using a pre-chamber as ignition source, based on the measurements in this paper, is shown in Figure 17 (excluding a potential post-engine N_2O removal system).

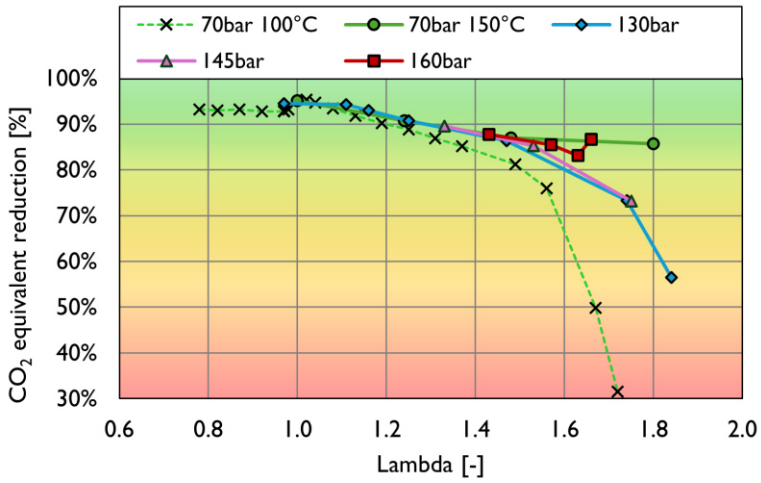

Figure 17: CO_2 reduction potential of a pre-chamber ignited ammonia engine without exhaust gas aftertreatment system based on N_2O emissions at different operating conditions.

However, the promising results of over 90% greenhouse gas emission reductions comparing to a methane burning engine for operating points with λ ≤ 1.2 support further investigations. Especially the possibility of N_2O catalyst systems should be considered. In addition, a diesel-like combustion scheme using a high-pressure direct ammonia injection in combination with a pilot injector is planned in comparison to the pre-chamber combustion concept presented here. Another study will investigate the addition of hydrogen to ammonia to facilitate the transition to completely carbon-free combustion.

Acknowledgments

Financial support from the Swiss Federal Office of Energy (SFOE, contract SI/502152-01) as well as funding by Winterthur Gas & Diesel (WinGD) is gratefully acknowledged.

Literature

[1] United Nations, "Paris Agreement", 2015, http://unfccc.int/files/essential_background/convention/application/pdf/english_paris_agreement.pdf.

[2] DNV Energy Transition Outlook 2020 (Det Norske Veritas), "*Maritime Forecast to 2050*".

[3] F. Abbasov, T. Earl; C. Calvo Ambel, B. Hemmings, L. Gilliam, "*Roadmap to decarbonising European shipping*". T&E - Transport & Environment, 2018.

[4] N. Ash, T. Scarbrough, "*Sailing on Solar – Could green ammonia decarbonise international shipping?*". Environmental Defense Fund, 2019.

[5] Lloyd's Register, UMAS (2019a), "*Fuel production cost estimates and assumptions*", Lloyd's Register; UMAS, 2019.

[6] Lloyd's Register, UMAS (2019b), "*Zero-Emission Vessels: Transition pathways*". Low Carbon Pathways 2050 series, Lloyd's Register; UMAS, 2019.

[7] Lloyd's Register; UMAS (2020), "*Techno-economic assessment of zero-carbon fuels*". Lloyd's Register; UMAS, 2020.

[8] P. Osterkamp, T. Smith, K. Søgaard, "*Five percent zero emission fuels by 2030 needed for Paris-aligned shipping decarbonization*", Global Maritime Forum. Getting to Zero Coalition (ed.), 2021.

[9] B. Schneider, C. Schürch, K. Boulouchos, S. Herzig, M. Hangartner, D. Humair, S. Wüthrich, C. Gossweiler, K. Herrmann, "*The Flex-OeCoS – a Novel Optically Accessible Test Rig for the Investigation of Advanced Combustion Processes under Engine-Like Conditions*", Energies 2020, 13(7), 1794; https://doi.org/10.3390/en13071794.

[10] S. Wüthrich, D. Humair, K. Herrmann, A. Bertola, "*Enhanced instrumentation of an optical research engine with unique combustion chamber*", 14th Int. AVL Symposium on Propulsion Diagnostics, June 23-24, 2020, Baden-Baden, Germany. ISBN 978-3-9816971-6-2.

[11] D. Humair, P. Cartier, P. Süess, S. Wüthrich, K. Herrmann, C. Barro, B. Schneider, C. Schürch, K. Boulouchos, "*Characterization of dual-fuel combustion processes*", Rostock 6th Large Engine Symposium, September 3-4, 2020, ISBN 978-3-941554-22-1.

[12] W. Vera-Tudela, B. Schneider, S. Wüthrich, K. Herrmann, "*Study on the ignitability of a high-pressure direct-injected methane jet using a diesel pilot, a glow-plug and a prechamber*", IJER-21-0139, 2021, https://doi.org/10.1177/14680874211048144.

[13] W. Vera-Tudela, B. Schneider, S. Wüthrich, K. Herrmann, "*Study on the ignitability of a high-pressure direct-injected methane jet using a scavenged pre-chamber under a wide range of conditions*", IJER-1-14, 2022, https://doi.org/10.1177/14680874221093144.

[14] S. Wüthrich, P. Cartier, P. Süess, B. Schneider, P. Obrecht, and K. Herrmann, "*Optical investigation and thermodynamic analysis of premixed ammonia dual-fuel combustion initiated by dodecane pilot fuel*", Fuel Communications 12 (2022) 100074, https://doi.org/10.1016/j.jfueco.2022.100074.

[15] J.M. Desantes, J.M. García-Oliver, W. Vera-Tudela, D. López-Pintor, B. Schneider, K. Boulouchos, "*Study of the auto-ignition phenomenon of PRFs under HCCI conditions in a RCEM by means of spectroscopy*", Applied Energy, Vol. 179, pp. 389-400, 2016, https://doi.org/10.1016/j.apenergy.2016.06.134.

[16] A. Srna, M. Bolla, Y.W. Wright, K. Herrmann, R. Bombach, S.S. Pandurangi, K. Boulouchos, G. Bruneaux, "*Ignition characteristics of n-dodecane pilot fuel spray in a premixed compressed methane/air charge*". Proceedings of the Combustion Institute 37 (2019) 4741–4749. https://doi.org/10.1016/j.proci.2018.06.177.

[17] J.M. Desantes, J.V. Pastor, J.M. García-Oliver, W. Vera-Tudela, "*An experimental study of the effects of fuel properties on reactive spray evolution using Primary Reference Fuels*", Fuel, Vol. 163, pp. 260-270, 2016, https://doi.org/10.1016/j.fuel.2015.09.064.

[18] A. Srna, R. Bombach, K. Herrmann, G. Bruneaux, "*Characterization of the spectral signature of dual-fuel combustion luminosity: implications for evaluation of natural luminosity imaging*", Applied Physics B (2019) 125:120, https://doi.org/10.1007/s00340-019-7222-z.

[19] P. Obrecht, "*WEG: calculation of the heat development law based on measured combustion chamber pressure traces*", in-house thermodynamic model, ETHZ-LAV & FHWN-ITFE, 2021.

[20] K. Herrmann, S. Wüthrich, P. Süess, P. Cartier, R. Moura, G. Weisser, "Initial investigations into ammonia combustion at conditions relevant for marine engines", CIMAC concress, June 12 – 16 2023, Busan

[21] S. Wüthrich, P. Albrecht, P. Cartier, and K. Herrmann, *„Comparison of Pilot Fuel Ignited Premixed Ammonia versus Methane Dual-Fuel Combustion",* 7th Large Engine Symposium, September 2022, Rostock, ISBN 978-3-941554-25-2

[22] J. Schramm, J. N. Klüssmann, L. R. Ekknud, A. Ivarsson, "*Ammonia Application in IC Engines*", 2020.

[23] C. Mounaïm-Rousselle, P. Bréquigny, C. Dumand, and S. Houillé, "*Operating Limits for Ammonia Fuel Spark-Ignition Engine*", Energies (14), 2021, https://doi.org/10.3390/en14144141.

[24] C. Lhuillier, P. Brequigny, F. Contino, and C. Mounaïm-Rousselle, "*Experimental study on ammonia/hydrogen/air combustion in spark ignition engine conditions*", Fuel (269), 2020, https://doi.org/10.1016/j.fuel.2020.117448.

[25] S. McAllister, J.-Y. Chen, and A. C. Fernandez-Pello, "*Fundamentals of Combustion Processes: Appendix*", New York, NY: Springer New York, 2011.

[26] S. Frankl, S. Gleis, S. Karmann, M. Prager, and G. Wachtmeister, "*Investigation of ammonia and hydrogen as CO2-free fuels for heavy duty engines using a high-pressure dual-fuel combustion process*", IJER, vol. 22, no. 10, pp. 3196–3208, Oct. 2021, https://doi.org/10.1177/1468087420967873.

[27] D. Han, Y. Liu, and Z. Huang, "*The Use of Ammonia as a Fuel for Combustion Engines*", Engines and Fuels for Future Transport, G. Kalghatgi, A. K. Agarwal, F. Leach, and K. Senecal, Eds. Singapore: Springer Singapore, 2022, pp. 233–256.

[28] R. Tanner, A. Guyer, W.D. Treadwell, "*Über die Verwendung von Ammoniak als Treibstoff*", *Eidgenössische technisch Hochschule in Zürich (ETHZ), Zürich 1945*